Journal of Energy Storage 58 (2023) 106333

Contents lists available at ScienceDirect

Journal of Energy Storage

journal homepage: www.elsevier.com/locate/est

Research papers

Artificial intelligence based nonlinear control of hybrid DC microgrid for dynamic stability and bidirectional power flow

Hafiz Muhammad Mehdi, Muhammad Kashif Azeem, Iftikhar Ahmad *

School of Electrical Engineering and Computer Science (SEECS), National University of Sciences and Technology (NUST), Islamabad, Pakistan

ARTICLE INFO

Keywords:
Microgrid (MG)
Hybrid energy storage system
Integral terminal sliding mode control
DC–DC converters
Battery electric vehicle (BEV)
Hardware in loop (HIL)

ABSTRACT

Conventional power generation resources are depleting rapidly and world power sector has been moving towards renewable energy sources (RESs). In this paper nonlinear control for renewable energy and hybrid energy storage system (HESS) based DC microgrid (DCMG) has been presented. PV and wind energy being the renewable sources whereas fuel cell, battery and ultracapacitor constitute the HESS. The global mathematical model of the said system has been presented. Datasets of varying solar irradiance and temperature have been trained by Artificial Neural Network for the reference voltage generation of PV. Integral terminal sliding mode controller (ITSMC) has been proposed for the output DC bus voltage regulation. Lyapunov stability criterion has ensured the overall stability of the system. A comparison of ITSMC with SMC and Lyapunov redesign controller has also been presented. Grid connected battery electric vehicle charger with grid to vehicle (G2V) and vehicle to grid modes (V2G) has been presented being an application of DCMG. The proposed system has been validated by using MATLAB/Simulink (2020b). Moreover, the hardware in loop setup has been used to observe the real time applicability of the proposed controller.

1. Introduction

Generation of electricity through conventional means especially from fossil fuels are the major concerns regarding the ongoing climatic conditions [1]. It is of quite concern for the researchers to pay attention towards the power generation by distributed generation system (DGS). It is referred to as solar and wind energy, also called clean energy. Being simple and energy efficient, renewable sources have gained much attention. The intermittent nature of renewable sources do not allow us to be used as alone power generation source [2,3]. Therefore, it is a conventional practice to use energy storage devices in parallel with renewable sources [4].

Hybrid energy storage system involves fuel cell, battery and ultra-capacitor. The combination of battery and ultra-capacitor is already studied in [4,5] but for such applications where a continuous supply of energy has been required irrespective of weather conditions, a source is mandatory which would be able to supply energy consistently. Fuel cell is a device which can combat with this situation [6]. So the combination of FC, battery and UC serve as an efficient energy storage system. Each source gives the micro solution to the drawback of other. Incompetence of battery is its low power density therefore it cannot combat with the load transients [7]. In this situation UC serves best because of its high power density [8]. Also the integration of UC increases the lifespan of battery [8]. Hence, the combination of DGS and HESS constitute the best topology for continuous power generation and storage.

Considering DGS, temperature and solar irradiance are the dependability factors of PV output whereas wind speed and torque measure the output in case of wind energy. For the optimization of output power of wind and PV in microgrid, these should be operated on maximum power point (MPP). There are many algorithms available in the literature for maximum power point tracking, for instance, artificial intelligence based algorithms [9], fuzzy logic control [10], linear and nonlinear controllers [11].

A microgrid can be DC, AC or the hybrid AC/DC microgrid. Many of the power electronics devices and modern load applications operate on DC power [12,13]. Being simple in structure, efficient and robust against external disturbances DCMGs gare gaining popularity. Moreover, the presence of reactive power and synchronization difficulty in AC or AC/DC microgrids motivate the researchers and end users to contribute in DCMGs [14,15] which are the best solution to provide power to remote area [7]. The control techniques that are available for AC microgrids in literature from [15–19] cannot be used for DCMG because of its different nature. An efficient energy management system and reliable control techniques are required for the smooth operation

* Corresponding author.
E-mail addresses: hmehdi.msee19seecs@seecs.edu.pk (H.M. Mehdi), mazeem.msee18seecs@seecs.edu.pk (M.K. Azeem), iftikhar.rana@seecs.edu.pk (I. Ahmad).

https://doi.org/10.1016/j.est.2022.106333
Received 14 January 2022; Received in revised form 25 July 2022; Accepted 3 December 2022
Available online 14 December 2022

Nomenclature

Acronyms

ADC	Analogue to digital converter
ANN	Artificial neural network
BEV	Battery electric vehicle
BS	Backstepping
CC	Constant current
CV	Constant voltage
DAC	Digital to analogue converter
$DCMG$	Direct current microgrid
DGS	Distributed generation system
$G2V$	Grid to vehicle
$HESS$	Hybrid energy storage system
HIL	Hardware in loop
$ITSMC$	Integral terminal sliding mode control
MCU	Micro-controller unit
MG	Microgrid
$MPPT$	Maximum power point tracking
OTC	Optimal torque control
$PMSG$	Permanent magnet synchronous generator
PV	Photovoltaic
$RESs$	Renewable energy sources
SCI	Serial communication interface
SMC	Sliding mode control
SoC	State of charge
$UART$	Universal asynchronous receiver transmitter
UC	Ultra-capacitor
UDR	Uncontrolled diode rectifier
$V2G$	Vehicle to grid
V_{MPP}	Maximum power point voltage

Indices

i	Index for error terms
k	Index for state variables
q	Index for sliding surfaces

Parameters

λ_{opt}	Optimum tip speed
ω_m	Angular speed of shaft
ρ	Air density
C_{p-max}	Maximum power co-efficient of turbine
T_{m-ref}	Maximum torque produced in turbine

Variables

I_{bat}	Battery current
I_{fc}	Fuel cell current
I_{pv}	Photovoltaic current
I_{uc}	Ultra-capacitor current
I_w	Wind current
V_{dc}	DC bus voltage
V_{pv}	Photovoltaic voltage

of DC microgrid. Regulation of output DC voltage is the foremost and core objective in DCMG [4].

In [20–22] many control techniques have been proposed for the output DC voltage regulation of DCMG despite the nonlinear nature of the system that mainly include DC–DC converters. The control technique that has been applied in [23] is the droop control. It becomes inefficient when multiple sources such as DGS and ESS are incorporated. Similarly, a control technique called H_∞ presented in [24] has considered the nonlinear behavior of the system due to the load fluctuation but no stability analysis has been done. A lot of work has been done in the area of DCMG to regulate the output DC voltage. The literature till now is based on linear controllers which do not perform efficiently in case of load transients due to the nonlinear behavior of converters.

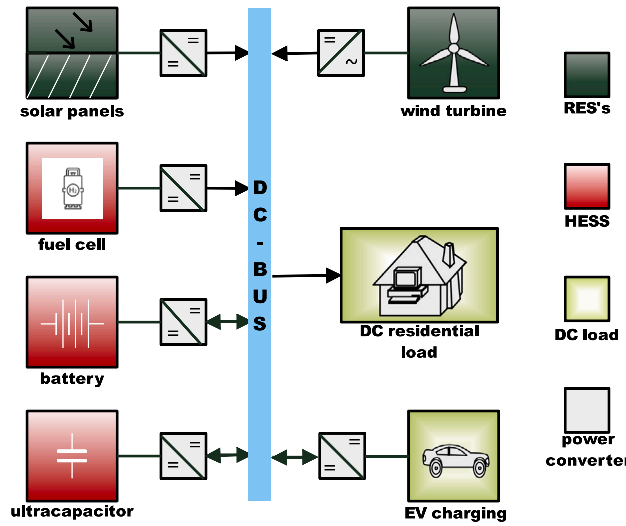

Fig. 1. Topology of considered DCMG.

A nonlinear control technique i.e. SMC presented in [25,26] for the regulation of output DC voltage. The results were satisfactory, but for the real time implementation this would not serve the purpose due to inherent phenomenon of chattering in SMC. In [27] a Finite time Adaptive SMC has been proposed to minimize the effect of disturbances caused by constant power load (CPL) and uncertainties to regulate the output voltage of DCMG. Backstepping control presented in [28] has not validated the affect of multiple sources on output voltage and whole system. The results of feedback linearization technique presented in [29] did not fulfill the criterion which make the system asymptotically stable. Also the output DC voltage showed fluctuations during load transients. In [30] Lyapunov redesign method has been considered for the output DC voltage regulation but the power of overall system has not been balanced. A novel control technique based on voltage variation has been proposed in [31] for a three source DCMG to incorporate the abrupt changes in load demand and suggested an improved power control method during both grid connected and island mode of operation but still the chattering problem is there which has to be removed by proposing an advanced nonlinear controller. A fuzzy logic based sliding mode control has been presented in [32] but the stability of DC bus voltage under intermittent nature of RESs has not been discussed. Similarly in [28,33–35] centralized and decentralized controllers have been discussed for the output voltage regulation of DCMG.

To address all the issues discussed above regarding the DC bus voltage regulation, an advanced and robust nonlinear controller has been needed. ITSMC has been proposed for the DC bus voltage regulation of considered DCMG having multiple input sources that include PV panels and wind turbine as RESs and FC, battery and UC as HESS. MPPT for the reference voltage generation of PV has been achieved by ANN using MATLAB by giving the data sets of varying solar irradiance and temperature.

In Fig. 1 topology of DC microgrid has been presented in which PV system is comprised of PV panels and DC–DC non-inverting buck-boost converter connected between DC bus and PV panels. Whereas

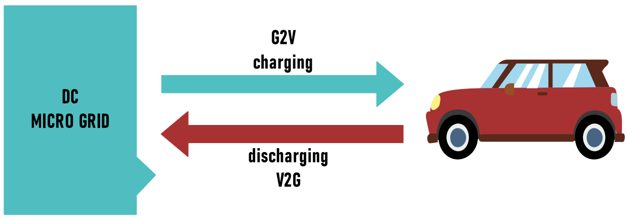

Fig. 2. Energy flow during charging and discharging of BEV.

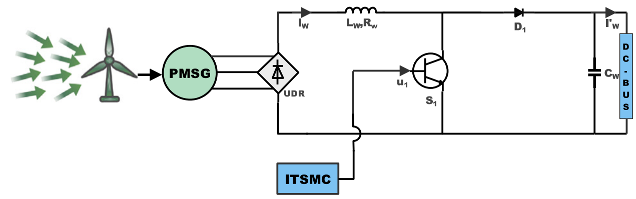

Fig. 3. Wind energy system.

Table 1
Wind energy system.

Wind turbine parameters	
Air density	1.225 kg/m^3
Rotor diameter	5.5 m
C_{p-max}	0.45
λ_{opt}	8.1
PMSG parameters	
Stator phase resistance	0.425 Ω
Armature inductance	0.000395 H
Flux linkage	0.433
Inertia	0.01197 kg/m^2
Viscous damping	0.001189 Nms

wind energy system is comprised of wind turbine, permanent magnet synchronous generator (PMSG), uncontrolled diode rectifier (UDR) and DC–DC boost converter. The converter has been connected between rectifier and DC bus. This constitutes a renewable based DGS. In the HESS, a DC–DC boost converter connected to fuel cell and DC–DC buck-boost converter has been connected to battery and UC to provide a bidirectional flow of current for charging and discharging purposes. HESS has been connected parallel to DGS, to overcome the stress on renewable sources during high load demand and to provide a continuous power to load in the absence of input from RESs during drastic weather conditions.

A lot of study has been carried out on the charging mechanism of electric vehicles. In [36–42] single and three phase chargers have been studied. The control techniques applied for charging of EV available in the literature are fuzzy logic control [42], PI control in [36–42] and optimal quadratic control [43]. In this paper both grid to vehicle (G2V) and vehicle to grid (V2G) modes of operation of a BEV charger have been presented as shown in Fig. 2. The G2V mode depicts the charging of vehicle, whereas the V2G mode depicts discharging. Flow of energy between grid and vehicle depend upon the SoC of BEV. The DC bus and EV charger have been connected through a non-inverting DC–DC boost-buck converter.

Main objectives of this research work are:

(1) Regulation of the output DC bus voltage at the desired value
(2) Generation and tracking of PV voltage at maximum power point using ANN
(3) Tracking of fuelcell current (I_{fc}), battery current (I_{bat}) and ultracapacitor current (I_{uc}) to their reference values to minimize the stress on renewable energy sources
(4) To ensure the safe charging and discharging of BEV during G2V and V2G mode respectively
(5) To ensure the asymptotic stability of the whole system by using Lyapunov stability criterion
(6) Verification of real time applicability of the proposed controller through HIL

Furthermore, this research article has been arranged as follows; Section 2 contains the state dynamical model of DCMG and BEV charger. Section 3 presents the proposed controller design of the whole system. Section 4 presents the simulation results and their detailed analysis. Section 5 discusses the experimental results of output DC bus voltage regulation of DCMG. Finally, Section 6 concludes the research paper.

2. Mathematical modeling of DC grid

2.1. Modeling of wind energy system

Wind energy system considered in this paper consists of wind turbine, permanent magnet synchronous generator (PMSG), uncontrolled diode rectifier and DC–DC boost converter as shown in Fig. 3. The wind turbine rotate under the air pressure. The mechanical energy of wind turbine is then converted into the electrical energy by PMSG. The alternating voltage signals obtained at the output of PMSG are then fed to the UDR which converts the AC into DC which is then fed to the DC–DC converter. The shaft speed and power generated by wind turbine change with the wind speed. That is why, optimal torque control (OTC) has been applied to extract maximum power continuously by MPPT [44].

The reference wind current at MPP can be obtained by the formula:

$$I_{ref} = \frac{t_{m-ref} * w_m}{v_d} \tag{1}$$

where v_d and w_m represent the rectified voltage and angular shaft speed respectively. Maximum torque t_{m-ref} gained by wind turbine under optimal conditions can be calculated using the following formula:

$$T_{m-ref} = 0.5\rho r^5 \pi \frac{C_{p-max}}{\lambda_{opt}^3} w_m^2 \tag{2}$$

where, ρ (kg/m^3) represents air density, r (m) is radius of turbine, C_{p-max} is the maximum power co-efficient of turbine, λ_{opt} is the optimum tip speed ratio that is dependent on the speed of shaft w_m (m/s). It has been assumed that operating mode of turbine is continuous conduction mode which act as apparent load for the generator. Boost converter consists of input inductor L_w, with the series resistance R_w, diode D_1, output filter capacitor C_w and IGBT acts as switch S_1.

All the parameters of wind energy system have been listed in Table 1 [45]. Following set of differential equations represent the state model of wind system [45].

$$\frac{dI_w}{dt} = \frac{V_{in}}{L_w} - I_w\frac{R_w}{L_w} - (1-u_1)\frac{V_w}{L_w} \tag{3}$$

$$\frac{dV_w}{dt} = (1-u_1)\frac{I_w}{C_w} - \frac{I'_w}{C_w} \tag{4}$$

I_w, V_{in} and V_w represent the wind input current, wind rectified input voltage and wind output voltage respectively. Whereas, u_1 represent the control signal to be generated by the proposed controller.

2.2. Modeling of PV energy system

The PV system considered in this research consist of PV array and a DC–DC non-inverting buck-boost converter as shown in Fig. 4. All the parameters of PV energy system have been listed in Table 3 [45]. In order to extract the maximum power from PV array, ANN algorithm has been used for the generation of PV reference voltage (V_{pvref}) against the varying solar temperature and irradiance. Following is the equation

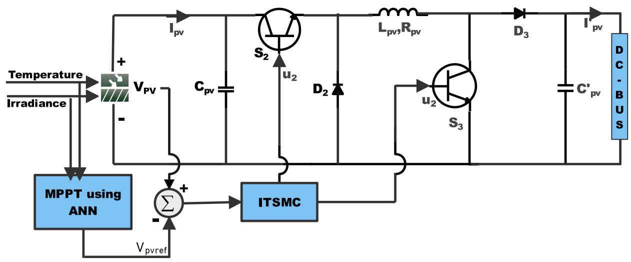

Fig. 4. PV energy system.

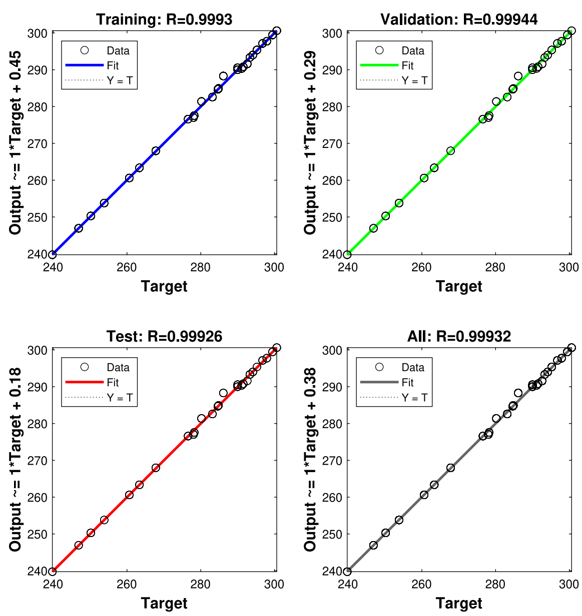

Fig. 5. Training, validation and test results for regression of the ANN model.

from which $Vpvref$ can be obtained for any value of solar temperature and irradiance [45].

$$V_{pvref} = 322 - (1.34 * Temperature) - (0.00964 * Irradiance) \tag{5}$$

Fig. 4 represents the DC–DC non-inverting buck-boost converter connected to the PV array. The switches S_2, S_3 represent two IGBTs and D_2, D_3 represent two diodes. L_{pv}, C_{pv} and C'_{pv} represent an inductor, input and output filtering capacitors respectively. It is assumed that mode of operation of the converter is continuous conduction mode (CCM). The controller generates the PWM signal which decides the ON and OFF time of the converter switches. The system operates in OFF load condition when both the switches S_2, S_3 are ON and the diode D_2 is operating in reverse biased mode. Contrary to it, the system operates in ON load condition when both the switches S_2, S_3 are OFF and the diode D_2 is operating in forward-biased mode and the output is taken across the filtering capacitor C'_{pv}.

Training of neural network has been carried out in MATLAB^R (2020b) using Levenberg–Marquardt algorithm. It is comprised of three layers i.e. input, output and hidden layer. Six neurons were used in the training process. Regression plot of the training data has been shown in Fig. 5 which depicts the perfect correlation between the trained and target data. In Table 2 the trained output of V_{MPP} against varying temperature and irradiance has been presented. The values of V_{MPP} obtained from neural network are very close to the target values which depicts the efficient response of ANN algorithm against the perturb and observe based MPPT algorithm.

Table 2
PV voltage comparison.

Irradiance (W/m^2)	Temperature (°C)	V_{MPP}(Actual) (V)	V_{MPP}(ANN) (V)
630	22	293.9856	294.2568
700	27	288.3241	288.5688
800	33	280.0023	280.1123
900	37	272.1248	272.5681
1000	42	267.3522	266.7164
850	36	275.1425	274.9148
720	33	277.1259	278.0043
610	30	283.0147	283.5699
510	28	286.5487	287.0263
440	25	288.9564	289.3528

Table 3
PV energy system.

PV array specifications	
PV module per string	10
Parallel connected strings	1
No. of cells permodule	60
Open circuit voltage	363 V
Short circuit current	7.84 A
Voltage at MPP	290 V
Current at MPP	7.35 A
Maximum power per module	2.1 kW

Following set of differential equations represent the state model of PV system [45];

$$\frac{dV_{pv}}{dt} = \frac{I_{pv}}{C_{pv}} - u_2 \frac{I_L}{C_{pv}} \tag{6}$$

$$\frac{dI_L}{dt} = u_2 \frac{V_{pv}}{L_{pv}} + u_2 \frac{V'_{pv}}{L_{pv}} - \frac{V'_{pv}}{L_{pv}} \tag{7}$$

$$\frac{dV'_{pv}}{dt} = \frac{I_L}{C_{pout}} - \frac{I'_{pv}}{C'_{pv}} - u_2 \frac{I_L}{C'_{pv}} \tag{8}$$

In the above dynamical equations, V_{pv}, I_L, V'_{pv} and I'_{pv} represent the PV input voltage, input current, PV output voltage and output current of the DC converter respectively. Control signal to be generated by the proposed controller has been represented by u_2.

2.3. Modeling of HESS

Hybrid energy storage system consists of fuel cell, battery and ultracapacitor. The parameters of storage devices have been listed in Table 4 [4]. Fuel cell has been connected to DC bus through a DC–DC boost converter. Elements of boost converter include a IGBT which act as a switch S_4, an inductor L_{fc} with a series resistance R_{fc} and an output filtering capacitor C_{fc} as shown in Fig. 6. The mathematical equations representing the boost converter are [4]:

$$\frac{dI_{fc}}{dt} = \frac{V_{fc}}{L_{fc}} - I_{fc}\frac{R_{fc}}{L_{fc}} - (1-u_3)\frac{V_{fc}}{L_{fc}} \tag{9}$$

$$\frac{dV_{fc}}{dt} = (1-u_3)\frac{I_{fc}}{C_{fc}} - \frac{I'_{fc}}{C_{fc}} \tag{10}$$

Here, V_{fc}, I_{fc} and I'_{fc} represent the input voltage of fuel cell, input current and output current of the boost converter respectively connected to the fuel cell. Whereas, u_3 is the PWM signal to control the ON and OFF position of the switch S_4.

Similarly, battery and ultracapacitor have been connected to DC bus through a bidirectional DC–DC buck-boost converter as their state of charge (SoC) vary depending upon the load current. The converter connected to battery include two IGBTs acting as switches S_5, S_6, an inductor L_{bat} with a series resistance R_{bat} and output filtering capacitor C_{bat}. When the battery contributes in fulfilling the load demand, it is called discharging mode i.e. $I_{bat} > 0$ and when $I_{bat} < 0$ that is called

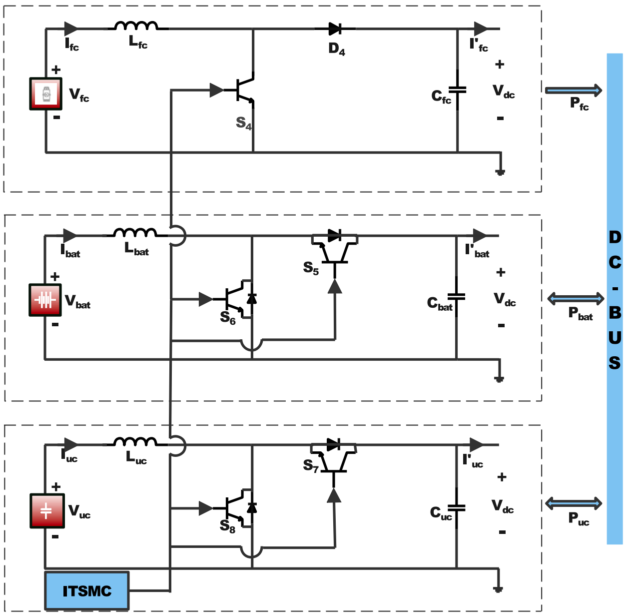

Fig. 6. Hybrid energy storage system.

charging mode of battery. The mathematical representation of these modes is as follows:

$$L = \begin{cases} 1, & \text{if } (I_{batref} > 0) \\ 0, & \text{if } (I_{batref} < 0) \end{cases} \tag{11}$$

I_{batref} is the reference current of battery. During the discharging mode, the converter has been modeled as:

$$\frac{dI_{bat}}{dt} = \frac{V_{bat}}{L_{bat}} - I_{bat}\frac{R_{bat}}{L_{bat}} - (1-u_4)\frac{V_{bat}}{L_{bat}} \tag{12}$$

$$\frac{dV_{bat}}{dt} = (1-u_4)\frac{I_{bat}}{C_{bat}} - \frac{I'_{bat}}{C_{bat}} \tag{13}$$

where, I_{bat} and I'_{bat} represent the battery and converter current respectively. Similarly, during charging mode, the converter has been modeled as:

$$\frac{dI_{bat}}{dt} = \frac{V_{bat}}{L_{bat}} - I_{bat}\frac{R_{bat}}{L_{bat}} - u_5\frac{V_{bat}}{L_{bat}} \tag{14}$$

$$\frac{dV_{bat}}{dt} = u_5\frac{I_{bat}}{C_{bat}} - \frac{I'_{bat}}{C_{bat}} \tag{15}$$

In order to make the model simple, following virtual control has been used:

$$u_{45} = [L(1-u_4) + (1-L)u_5] \tag{16}$$

From Eqs. (12)–(16) the battery converter can be modeled as:

$$\frac{dI_{bat}}{dt} = \frac{V_{bat}}{L_{bat}} - I_{bat}\frac{R_{bat}}{L_{bat}} - u_{45}\frac{V_{bat}}{L_{bat}}] \tag{17}$$

$$\frac{dV_{bat}}{dt} = u_{45}\frac{I_{bat}}{C_{bat}} - \frac{I'_{bat}}{C_{bat}} \tag{18}$$

Similarly, ultracapacitor connected to DC bus through a DC–DC buck-boost converter also has two modes i.e. charging and discharging, expressed as:

$$M = \begin{cases} 1, & \text{if } (I_{ucref} > 0) \\ 0, & \text{if } (I_{ucref} < 0) \end{cases} \tag{19}$$

The dynamical equations that express the discharging mode of UC are:

$$\frac{dI_{uc}}{dt} = \frac{V_{uc}}{L_{uc}} - I_{uc}\frac{R_{uc}}{L_{uc}} - (1-u_6)\frac{V_{uc}}{L_{uc}} \tag{20}$$

Table 4
Hybrid energy storage system.

Fuel cell parameters	
Voltage	262 V
Rated capacity	20 kW
Lithium ion battery	
Voltage	540 V
Rated capacity	33.9 Ah
Maximum charge current	17.5 A
Maximum discharge current	30 A
Ultracapacitor	
Voltage	205 V
Rated capacity	2700 F

$$\frac{dV_{uc}}{dt} = (1-u_6)\frac{I_{uc}}{C_{uc}} - \frac{I'_{uc}}{C_{uc}} \tag{21}$$

where, I_{uc} and I'_{uc} are the currents of ultracapacitor and converter output. Similarly, following dynamical equations express the charging mode of UC:

$$\frac{dI_{uc}}{dt} = \frac{V_{uc}}{L_{uc}} - I_{uc}\frac{R_{uc}}{L_{uc}} - u_7\frac{V_{uc}}{L_{uc}} \tag{22}$$

$$\frac{dV_{uc}}{dt} = u_7\frac{I_{uc}}{C_{uc}} - \frac{I'_{uc}}{C_{uc}} \tag{23}$$

For simplification, virtual control has been represented by:

$$u_{67} = [M(1-u_6) + (1-M)u_7] \tag{24}$$

From Eqs. (20)–(24) converter model for ultracapacitor has been expressed as:

$$\frac{dI_{uc}}{dt} = \frac{V_{uc}}{L_{uc}} - I_{uc}\frac{R_{uc}}{L_{uc}} - u_{67}\frac{V_{uc}}{L_{uc}} \tag{25}$$

$$\frac{dV_{uc}}{dt} = u_{67}\frac{I_{uc}}{C_{uc}} - \frac{I'_{uc}}{C_{uc}} \tag{26}$$

2.4. Global mathematical model of the DC microgrid

$$\dot{x}_1 = \frac{V_{in}}{L_w} - x_1\frac{R_w}{L_w} - (1-u_1)\frac{x_7}{L_w} \tag{27}$$

$$\dot{x}_2 = \frac{I_{pv}}{C_{pv}} - u_2\frac{x_3}{C_{pv}} \tag{28}$$

$$\dot{x}_3 = u_2\frac{x_2}{L_{pv}} - (1-u_2)\frac{x_7}{L_{pv}} \tag{29}$$

$$\dot{x}_4 = \frac{V_{fc}}{L_{fc}} - x_4\frac{R_{fc}}{L_{fc}} - (1-u_3)\frac{x_7}{L_{fc}} \tag{30}$$

$$\dot{x}_5 = \frac{V_{bat}}{L_{bat}} - x_5\frac{R_{bat}}{L_{bat}} - u_{45}\frac{x_7}{L_{bat}} \tag{31}$$

$$\dot{x}_6 = \frac{V_{uc}}{L_{uc}} - x_6\frac{R_{uc}}{L_{uc}} - u_{67}\frac{x_7}{L_{uc}} \tag{32}$$

$$\dot{x}_7 = (1-u_1)\frac{x_1}{C_{dc}} + (1-u_2)\frac{x_3}{C_{dc}} + (1-u_3)\frac{x_4}{C_{dc}} + u_{45}\frac{x_5}{C_{dc}} + u_{67}\frac{x_6}{C_{dc}} - \frac{I_o}{C_{dc}} \tag{33}$$

Eqs. (27)–(33) represent the global mathematical model of DC microgrid by where, x_1, x_2, x_3, x_4, x_5, x_6 and x_7 represents I_w, V_{pv}, I_{pv}, I_{fc}, I_{bat}, I_{uc} and V_{dc} respectively. Whereas, u_1, u_2, u_3, u_{45} and u_{67} are the control signals of the whole system which are responsible for the regulation of output DC bus voltage and respective current of power sources.

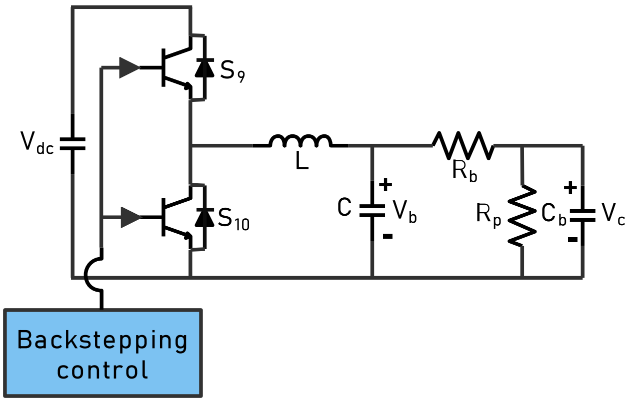

Fig. 7. Battery connected bidirectional DC–DC converter.

2.5. Modeling of grid connected BEV charger

An on-board charger of battery electric vehicle has been presented in this paper as an application of DCMG. In Fig. 7 the DC–DC buck-boost converter has been connected with DC bus followed by the thevinen circuit of battery [43] on the load side. The power converter consists of two IGBTs which act as switches S_9, S_{10}, an inductor L and an output filtering capacitor C. The converter is capable of working on both the modes i.e buck and boost depending upon the flow of energy i.e from DC bus to battery or vice-versa. The thevinen circuit of battery consist of a capacitor C_b and two resistors i.e. R_b and R_p. R_b represents the equivalent series resistance of plate grids, interconnecting conductors and electrolyte. Whereas, R_p is the equivalent parallel resistance that represent the impurities present in electrolyte and plates of battery. These impurities are responsible for the self discharge of battery during open circuit. Battery capacitance is represented by C_b. The operating modes of converter associated with the BEV charger are:

$$S = \begin{cases} 1, & \text{G2V mode} \\ 0, & \text{V2G mode} \end{cases} \tag{34}$$

The control signal for the switching of IGBTs of converter can be taken as:

$$u_{89} = Su_8 + (1-S)(1-u_9) \tag{35}$$

Following is the set of dynamical equations that represent the model of BEV charger:

$$\dot{x}_8 = \frac{-x_9}{L} + u_{89}\frac{V_{dc}}{L} \tag{36}$$

$$\dot{x}_9 = \frac{x_8}{C} - \frac{x_9}{R_bC} + \frac{x_{10}}{R_bC} \tag{37}$$

$$\dot{x}_{10} = \frac{x_9}{R_bC_b} - \frac{x_{10}}{R_bC_b} - \frac{x_{10}}{R_pC_b} \tag{38}$$

where, x_8, x_9 and x_{10} represent the inductor current I_L, battery outer voltage V_b and battery inner voltage V_c respectively.

3. Controller design

In this section control laws have been derived for the output DC bus voltage regulation of DCMG by using ITSMC. Whereas, Backstepping (BS) control has been presented to obtain the control law of grid connected BEV charger. Since the multiple input system is under consideration having non-minimum phase nature. So it is suggested to control the output DC bus voltage indirectly through current except PV system. Here we need to track the fuel cell current to its reference value which in turn regulate the output DC bus voltage. Power balance equation shows the relation of fuel cell current and DC bus voltage as:

$$P_{in} = P_{out} \tag{39}$$

$$V_{in}I_{wref} + V_{pvref}I_{pv} + V_{fc}I_{fcref} + V_{bat}I_{batref} + V_{uc}I_{ucref} = V_{dc}I_o \tag{40}$$

$$I_{fcref} = \delta\left(\frac{V_{dc}I_o - V_{in}I_{wref} - V_{pvref}I_{pv} - V_{bat}I_{batref} - V_{uc}I_{ucref}}{V_{fc}}\right) \tag{41}$$

where, δ is called ideality factor and its value varies with the efficiency of boost converter. In this paper we assume the 95 percent efficiency of boost converter so its value is 1.052 but in ideal case its value is taken as 1.

3.1. Control design for DC bus voltage regulation of DCMG

An integral terminal sliding mode control technique is known for its better results. Chattering phenomenon in ITSMC is negligible as compared to SMC. For the tracking of DC bus voltage, the general error equation is taken as:

$$e_i = x_k - x_{kref} \tag{42}$$

where, (i = 1 to 5) representing the six error terms and $k = 1, 2, 4, 5$ and 6 representing I_w, V_{pv}, I_{fc}, I_{bat} and I_{uc} respectively. Time derivative of the error equation yields:

$$\dot{e}_i = \dot{x}_k - \dot{x}_{kref} \tag{43}$$

The number of integral terminal surfaces depend upon the number of control inputs. The surfaces are defined as:

$$S_i = e_i + K_i\left(\int_0^t e_i dt\right)^{\gamma_i} \tag{44}$$

where, K_i is the design parameter and its value is always positive. The value of γ_i is always in between 0 and 1. Taking the time derivative of Eq. (44) yields:

$$\dot{S}_i = \dot{e}_i + \gamma_i K_i e_i\left(\int_0^t e_i dt\right)^{\gamma_i - 1} \tag{45}$$

By substituting the values of $\dot{e}_i$ from Eq. (43) we get:

$$\dot{S}_1 = \left(\frac{V_{in}}{L_w} - x_1\frac{R_w}{L_w} - (1-u_1)\frac{x_7}{L_w} - \dot{I}_{wref} + \gamma_1K_1e_1\left(\int_0^t e_1 dt\right)^{\gamma_1-1}\right) \tag{46}$$

$$\dot{S}_2 = \left(\frac{I_{pv}}{C_{pv}} - u_2\frac{x_3}{C_{pv}} - \dot{V}_{pvref} + \gamma_2K_2e_2\left(\int_0^t e_2 dt\right)^{\gamma_2-1}\right) \tag{47}$$

$$\dot{S}_3 = \left(\frac{V_{fc}}{L_{fc}} - x_4\frac{R_{fc}}{L_{fc}} - (1-u_3)\frac{x_7}{L_{fc}} - \dot{I}_{fcref} + \gamma_3K_3e_3\left(\int_0^t e_3 dt\right)^{\gamma_3-1}\right) \tag{48}$$

$$\dot{S}_4 = \left(\frac{V_{bat}}{L_{bat}} - x_5\frac{R_{bat}}{L_{bat}} - (u_{45})\frac{x_7}{L_{bat}} - \dot{I}_{batref} + \gamma_4K_4e_4\left(\int_0^t e_4 dt\right)^{\gamma_4-1}\right) \tag{49}$$

$$\dot{S}_5 = \left(\frac{V_{uc}}{L_{uc}} - x_6\frac{R_{uc}}{L_{uc}} - (u_{67})\frac{x_7}{L_{uc}} - \dot{I}_{ucref} + \gamma_5K_5e_5\left(\int_0^t e_5 dt\right)^{\gamma_5-1}\right) \tag{50}$$

In order to fulfill the Lyapunov stability criterion, we enforce all the surfaces $\dot{S}_q$ to behave as:

$$\dot{S}_q = -\rho_q sgn(S_q) \tag{51}$$

where $\rho_q > 0$ and q = 1 to 5. sgn is known as the signum function defined as:

$$Sgn(y) = \begin{cases} \frac{y}{|y|}, & y \neq 0 \\ 0, & y = 0 \end{cases} \tag{52}$$

By comparing the set of Eqs. (47)–(51) with Eq. (52), we get the following control laws:

$$u_1 = 1 - \frac{L_w}{x_7}\left[\frac{V_{in}}{L_w} - x_1\frac{R_w}{L_w} - \dot{I}_{wref} + \gamma_1 K_1 e_1\left(\int_0^t e_1 dt\right)^{\gamma_1 - 1} + \rho_1 Sgn(S_1)\right] \tag{53}$$

$$u_2 = \frac{C_{pv}}{x_3}\left[\frac{I_{pv}}{C_{pv}} - \dot{V}_{pvref} + \gamma_2 K_2 e_2\left(\int_0^t e_2 dt\right)^{\gamma_2 - 1} + \rho_2 Sgn(S_2)\right] \tag{54}$$

$$u_3 = 1 - \frac{L_{fc}}{x_7}\left[\frac{V_{fc}}{L_{fc}} - x_4\frac{R_{fc}}{L_{fc}} - \dot{I}_{fcref} + \gamma_3 K_3 e_3\left(\int_0^t e_3 dt\right)^{\gamma_3 - 1} + \rho_3 Sgn(S_3)\right] \tag{55}$$

$$u_{45} = \frac{L_{bat}}{x_7}\left[\frac{V_{bat}}{L_{bat}} - x_5\frac{R_{bat}}{L_{bat}} - \dot{I}_{batref} + \gamma_4 K_4 e_4\left(\int_0^t e_4 dt\right)^{\gamma_4 - 1} + \rho_4 Sgn(S_4)\right] \tag{56}$$

$$u_{67} = \frac{L_{uc}}{x_7}\left[\frac{V_{uc}}{L_{uc}} - x_6\frac{R_{uc}}{L_{uc}} - \dot{I}_{ucref} + \gamma_5 K_5 e_5\left(\int_0^t e_5 dt\right)^{\gamma_5 - 1} + \rho_5 Sgn(S_5)\right] \tag{57}$$

where, u_1, u_2, u_3, u_{45} and u_{67} are the duty cycles of the converters connected to wind, PV, FC, battery and UC respectively. All the duty cycles are bounded between 0 and 1.

Now, to check the stability of the whole system, a positive definite Lyapunov candidate function V has been introduced as:

$$V = \frac{1}{2}S_1^2 + \frac{1}{2}S_2^2 + \frac{1}{2}S_3^2 + \frac{1}{2}S_4^2 + \frac{1}{2}S_5^2 \tag{58}$$

The time derivative of the V must be negative definite to prove the asymptotic stability of the system. So, taking the time derivative of Eq. (59) gives:

$$\dot{V} = S_1\dot{S}_1 + S_2\dot{S}_2 + S_3\dot{S}_3 + S_4\dot{S}_4 + S_5\dot{S}_5 \tag{59}$$

Substituting the values of $\dot{S}_q$ we get:

$$\dot{V} = (-\rho_1|S_1| - \rho_2|S_2| - \rho_3|S_3| - \rho_4|S_4| - \rho_5|S_5|) \le 0 \tag{60}$$

Hence, the stability of the proposed controller has been proved by Lyapunov stability criterion.

3.2. Control design of grid connected BEV charger

A Backstepping control technique has been proposed in this paper for the safe operation of an on board battery electric vehicle charger connected to the DC microgrid. BS is known for its definite tracking property [46]. G2V mode of operation corresponds to the charging of battery, whereas discharging corresponds to V2G mode. Charging process has been carried out in both stages i.e. constant current (CC) and constant voltage (CV). Whereas battery discharging has been done only in CC stage by giving a negative current reference.

3.2.1. Constant current stage

During CC stage, battery current I_b can be track to its reference value I_{b*} by taking its error e_7:

$$e_7 = I_b - I_b^* \tag{61}$$

Implication of Kirchhoff's voltage law on Fig. 7 gives the following expression of battery current I_b as:

$$e_7 = \frac{1}{R_b}(x_9 - x_{10}) - I_b^* \tag{62}$$

Taking the time derivative of Eq. (63) and assuming $\dot{I}_b^* \approx 0$ yields:

$$\dot{e}_7 = \frac{1}{R_b C}x_8 - \frac{y}{R_b}x_9 + \frac{z}{R_b}x_{10} \tag{63}$$

where,

$$y = \frac{1}{R_b C} + \frac{1}{R_b C_b} \tag{64}$$

$$z = y + \frac{1}{R_p C_b} \tag{65}$$

Here, we consider a Lyapunov candidate function as:

$$V_7 = \frac{1}{2}e_7^2 \tag{66}$$

Taking the time derivative of V_7 yields $\dot{V}_7 = e_7\dot{e}_7$. In order to enforce e_7 to vanish exponentially, we consider:

$$\dot{e}_7 = -c_7 e_7 \tag{67}$$

where, $c_7 > 0$ is the design parameter. The expression ($\alpha = x_8/R_b C$) is considered as a virtual control. By comparing Eqs. (64) and (68), α has been expressed as:

$$\alpha = -c_7 e_7 + \frac{y}{R_b}x_9 - \frac{z}{R_b}x_{10} \tag{68}$$

Assigning a new error term to the virtual control ($\alpha = x_8/R_b C$) as:

$$e_8 = \frac{x_8}{R_b C} - \alpha \tag{69}$$

By using Eq. (64), Eqs. (69) and (70) we get:

$$\dot{e}_7 = -c_7 e_7 + e_8 \tag{70}$$

Substituting the value of $\dot{e}_7$ in $\dot{V}_7$ yields:

$$\dot{V}_7 = -c_7 e_7^2 + e_7 e_8 \tag{71}$$

From Eqs. (69) and (70) $\dot{e}_8$ is expressed as:

$$\dot{e}_8 = \frac{1}{R_b C}\dot{x}_8 + c_7\dot{e}_7 - \frac{y}{R_b}\dot{x}_9 + \frac{z}{R_b}\dot{x}_{10} \tag{72}$$

Considering the Lyapunov candidate function as:

$$V_8 = V_7 + \frac{1}{2}e_8^2 \tag{73}$$

Since, the objective is to derive the errors e_7 and e_8 to zero, taking time derivative of Eq. (74) and using Eq. (72) yields:

$$\dot{V}_8 = -c_7 e_7^2 + e_8(e_7 + \dot{e}_8) \tag{74}$$

Assume $\dot{e}_8 = -c_8 e_8 - e_7$ to make $\dot{V}_8$ negative definite i.e:

$$\dot{V}_8 = -c_7 e_7^2 - c_8 e_8^2 \tag{75}$$

where, $c_8 > 0$ is the design parameter. Eq. (76) shows the asymptotic stability of the system and the error terms e_7 and e_8 clearly decay to zero. From Eqs. (69) and (73):

$$\frac{\dot{x}_8}{R_b C} = -c_8 e_8 - e_7 - c_7\dot{e}_7 + \frac{y}{Rb}\dot{x}_9 - \frac{z}{Rb}\dot{x}_{10} \tag{76}$$

From Eqs. (36)–(38), Eqs. (71) and (77) the control law u_{89} for the power converter connected to battery of EV and DC bus during CC stage can be obtained as:

$$u_{89} = \frac{1}{V_{dc}}\left[m_1 e_7 + m_2 e_8 + m_3 x_8 + m_4 x_9 + m_5 x_{10}\right] \tag{77}$$

where,

$$m_1 = -(1 - c_7^2)LCR_b \tag{78}$$

$$m_2 = -(c_7 + c_8)LCR_b \tag{79}$$

$$m_3 = y * L \tag{80}$$

$$m_4 = 1 - \left(\frac{y}{R_b C} + \frac{z}{R_b C_b}\right)LC \tag{81}$$

$$m_5 = \left[\frac{y}{R_b C} + \left(\frac{z}{R_b C_b} + \frac{z}{R_p C_b}\right)\right]LC \tag{82}$$

3.2.2. Constant voltage stage

The control objective of CV stage is to keep the battery voltage V_b equal to the reference voltage V_b^*. For this purpose the error term is introduced as:

$$e_9 = x_9 - V_b^* \tag{83}$$

Assume $\dot{V}_b \approx 0$, the time derivative of e_9 can be expressed as:

$$\dot{e}_9 = \frac{1}{C}x_8 - \frac{1}{R_bC}x_9 + \frac{1}{R_bC}x_{10} \tag{84}$$

Here, we consider a Lyapunov candidate function for the stability analysis as:

$$V_9 = \frac{1}{2}e_9^2 \tag{85}$$

Taking the time derivative of V_9 yields $\dot{V}_9 = e_9\dot{e}_9$. In order to enforce e_9 to vanish exponentially, we take:

$$\dot{e}_9 = -c_9e_9 \tag{86}$$

Where, $c_9 > 0$ is the design parameter. The expression ($\beta = x_8/C$) is considered as a virtual control. By comparing Eqs. (85) and (87), β can be expressed as:

$$\beta = -c_9e_9 + \frac{x_9}{R_bC} - \frac{x_{10}}{R_bC} \tag{87}$$

Assigning a new error term to the virtual control ($\beta = x_8/C$) as:

$$e_{10} = \frac{x_8}{C} - \beta \tag{88}$$

By using Eq. (85), Eqs. (88) and (89) we get:

$$\dot{e}_9 = -c_9e_9 + e_{10} \tag{89}$$

Substituting the value of $\dot{e}_9$ in the expression of $\dot{V}_9$ = yields:

$$\dot{V}_9 = -c_9e_9^2 + e_9e_{10} \tag{90}$$

From Eqs. (88) and (89), $\dot{e}_{10}$ can be expressed as:

$$\dot{e}_{10} = \frac{1}{R_bC}\dot{x}_8 + c_7\dot{e}_7 - \frac{y}{Rb}\dot{x}_9 + \frac{z}{Rb}\dot{x}_{10} \tag{91}$$

Considering the Lyapunov candidate function as:

$$V_8 = V_7 + \frac{1}{2}e_8^2 \tag{92}$$

Since, the objective is derive errors e_7 and e_8 to zero, taking the time derivative of V_8 yields:

$$\dot{V}_8 = -c_7e_7^2 + e_8(e_7 + \dot{e}_8) \tag{93}$$

Assume $\dot{e}_8 = -c_8e_8 - e_7$ to make $\dot{V}_8$ negative definite gives:

$$\dot{V}_8 = -c_7e_7^2 - c_8e_8^2 \tag{94}$$

where, $c_8 > 0$ is the design parameter. Eq. (95) shows the asymptotic stability of the system and the error terms e_7 and e_8 clearly decay to zero. From Eqs. (88) and (92), we can write:

$$\frac{\dot{x}_8}{C} = -c_{10}e_{10} - e_9 - c_9\dot{e}_9 + \frac{\dot{x}_9}{R_bC} - \frac{\dot{x}_{10}}{R_bC} \tag{95}$$

From Eqs. (36)–(38), Eqs. (87) and (96) the control law u_{89} for the power converter connected to battery of EV and DC bus during CV stage can be obtained as:

$$u_{89} = \frac{1}{V_{dc}}\left[n_1e_9 + n_2e_{10} + n_3x_8 + n_4x_9 + n_5x_{10}\right] \tag{96}$$

where,

$$n_1 = -(1 - c_9^2)LC \tag{97}$$

$$n_2 = -(c_9 + c_{10})LC \tag{98}$$

$$n_3 = \frac{L}{R_bC} \tag{99}$$

$$n_4 = 1 - \frac{yL}{R_b} \tag{100}$$

$$n_5 = \frac{zL}{R_b} \tag{101}$$

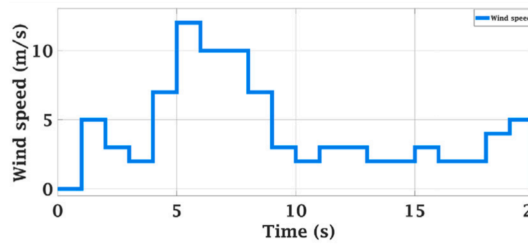

Fig. 8. Wind speed.

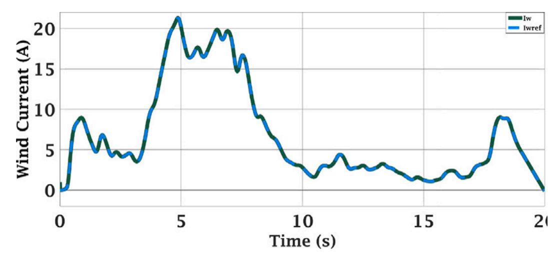

Fig. 9. Wind current (state $x_1 = I_w$).

4. Simulation results and analysis

The efficiency of proposed nonlinear controllers have been verified by simulating the global mathematical model of DCMG given by Eqs. (27)–(33) and model of grid connected BEV charger given by Eqs. (36)–(38) on MATLAB/Simulink. The simulation parameters of both the DCMG and EV charger have been listed in Table 5 and Table 6 respectively. The voltage and current specifications of all the sources used in this research work have been placed in Tables 2–4. In Figs. 8–23 and Figs. 24–28 simulation results of DCMG and EV charger have been presented. The detailed analysis of the results of output DC bus voltage regulation of DCMG have been presented in Section 4.1 whereas, in Section 4.2, the results of Backstepping control for both G2V and V2G modes of operation of grid connected EV charger have been presented. Section 4.1 has been further divided in two sub-parts, one for the constant and the second for varying load. The performance of proposed controller i.e. ITSMC has been tested under the varying conditions of wind speed, temperature, irradiance and resistive load. The results have been compared with SMC and Lyapunov redesign controllers. The results of wind speed and current obtained from control law given by Eq. (53) have been presented in Fig. 8 and Fig. 9 respectively. It is clear that wind speed and current are directly proportional to each other. At t = 5 s wind speed raised from 7 m/s to 12 m/s, the current also raised simultaneously. Similarly, when wind speed dropped from 7 m/s to 3 m/s at t = 9 s, the wind current also dropped. The results of PV voltage and current obtained from control law given in Eq. (54) have been presented in Figs. 10 and 11. The variation in PV temperature and irradiance have been noted from 22 ° C to 42 ° C and 440 W/m^2 to 1000 W/m^2 respectively given in Table 1. It is important to mention that power generated by PV array and PV temperature are inversely related to each other. [47–49] proposes the energy management system which can be used further as a benchmark for testing the functionality of the proposed model in the operational horizon.

4.1. Result analysis of proposed nonlinear controller for DCMG

4.1.1. Case 1

The value of load current has been fixed at 60 A in this case, presented in Fig. 12. The RESs are being operated in varying conditions of wind speed, temperature and irradiance. The regulation of output DC bus voltage has been carried out at 700 V by ITSMC and the results

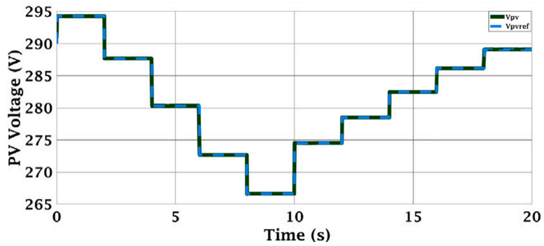

Fig. 10. PV voltage (state $x_2=V_{pv}$).

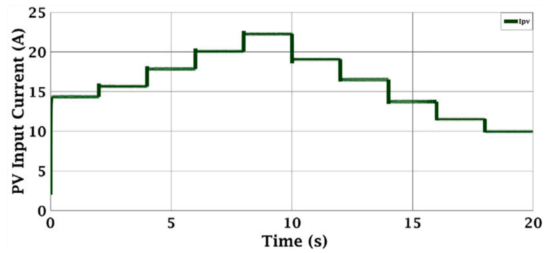

Fig. 11. PV current (state $x_3=I_{pv}$).

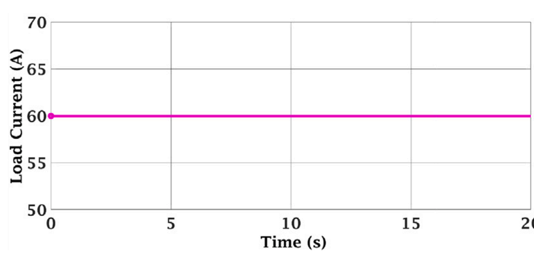

Fig. 12. Case 1: Load current.

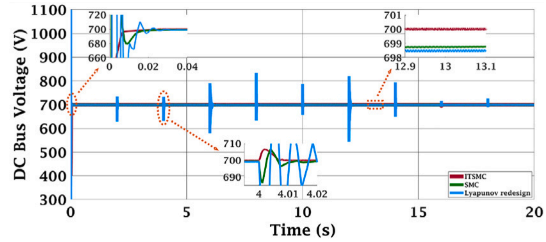

Fig. 13. Case 1: DC bus voltage (state $x_7=V_{dc}$).

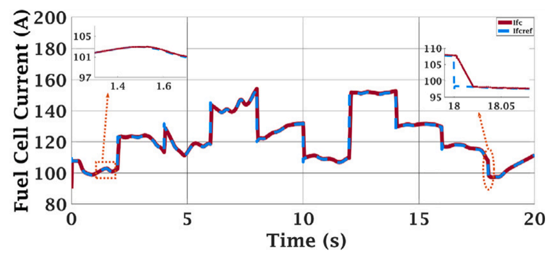

Fig. 14. Case 1: Fuel cell current (state $x_4=I_{fc}$).

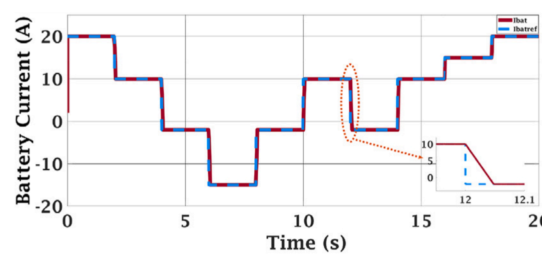

Fig. 15. Case 1: Battery current (state $x_5=I_{bat}$).

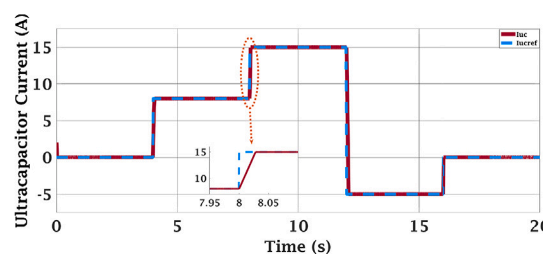

Fig. 16. Case 1: Ultracapacitor current (state $x_6=I_{uc}$).

are then compared with SMC and Lyapunov redesign controller for the detailed analysis. Fig. 13 depicts the high performance of ITSMC as no major overshoot or undershoot has been observed. At t = 4 s ITSMC showed an overshoot of 7 V whereas, SMC and Lyapunov redesign controller showed an undershoot of 12 V and 70 V respectively. Also, the SMC and Lyapunov redesign have shown the steady state error of 1.7 V and 2 V respectively as reflected from t = 12.9 s – 13.1 s. SMC is known for its ability to cater the disturbances but its poor performance in this case can be improved by using its higher order variant or by increasing its gains. But with a drawback that increase in the control effort results in computationally complex controller. Also the chattering is an inherent drawback of SMC. Figs. 14–16 depict the currents of FC, battery and UC. All the storage devices have ensured an accurate reference current tracking and worked within the prescribed limit. From the Figs. 9–16, it is obvious that fuel cell throughout shared the load with RESs. Battery has been operated in normal load conditions whereas, UC has been used to cater the load fluctuations. In Fig. 16 from t = 4 – 10 s, UC share the load of battery and goes in discharging mode during transients when the generation of renewable sources is decreased due to the weather conditions. This characteristic of UC ensures the increased life span of battery making the whole system economical. Similarly from t = 12 – 16 s UC goes in charging mode when RESs along with FC and battery start generating enough power to meet the load demand. The output DC bus voltage regulation with extremely negligible steady state error defines the effectiveness of proposed controller.

4.1.2. Case 2

The value of load current has been varied between 35 A and 60 A as shown in Fig. 17. The RESs are being operated in varying conditions of wind speed, temperature and solar irradiance. The output DC bus voltage has been regulated at 700 V by using ITSMC and other comparison controllers i.e. SMC and Lyapunov redesign controller as shown in Fig. 18. The results depicted far better performance of ITSMC than that of SMC and Lyapunov redesign as it showed an undershoot of few volts initially as shown in Fig. 18. Contrarily, SMC and Lyapunov redesign showed overshoots of 350 V and 450 V respectively from $t = 0 - 0.01$ s. Similar behavior has been observed at t = 18 s where ITSMC reflected minor undershoot due to the intermittent nature of RESs whereas SMC and Lyapunov redesign showed a markable overshoot of 70 V and an undershoot of 100 V respectively. It can be seen in Fig. 17 that when the high amount of load current was demanded from t = 8 – 12 s RESs could not meet the demand. At that instant FC fulfilled the demand with the assistance of both the battery and UC as shown in Figs. 19 and 20 which is highly appreciating. From $t = 12 - 16$ s, in Fig. 21 UC shifted to charging mode as the load demand being fulfilled by RESs along with FC and battery. Similarly, when the load demand in Fig. 17 decreased

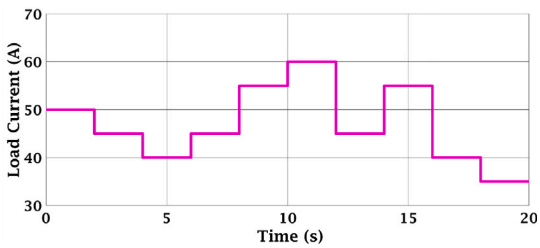

Fig. 17. Case 2: Load current.

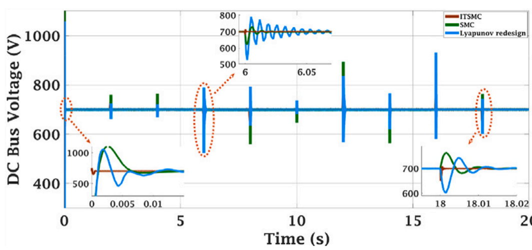

Fig. 18. Case 2: DC bus voltage (state $x_7=V_{dc}$).

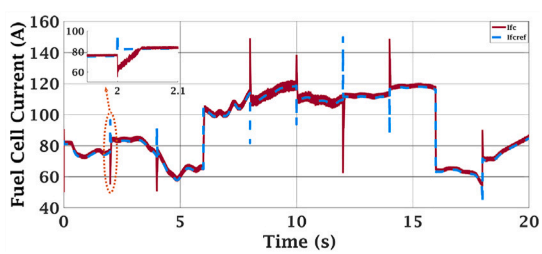

Fig. 19. Case 2: Fuel cell current (state $x_4=I_{fc}$).

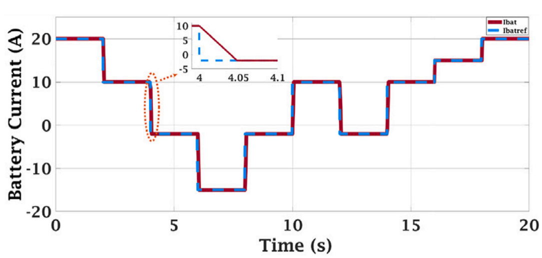

Fig. 20. Case 2: Battery current (state $x_5=I_{bat}$).

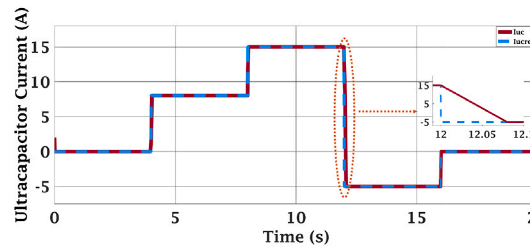

Fig. 21. Case 2: Ultracapacitor current (state $x_6=I_{uc}$).

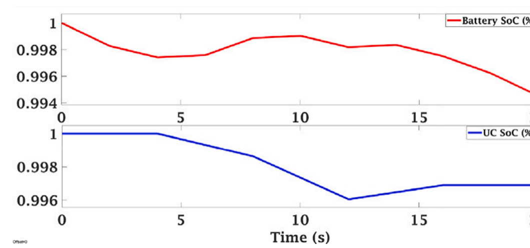

Fig. 22. Case 2:(a) SoC of battery, (b) SoC of Ultracapacitor.

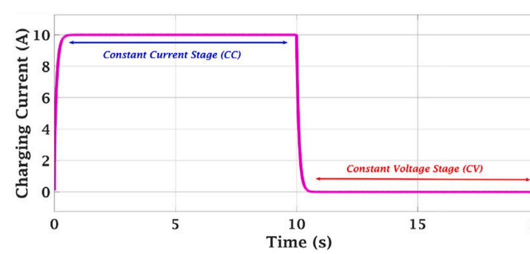

Fig. 23. Battery charging current; $I_b(G2V\,mode)$.

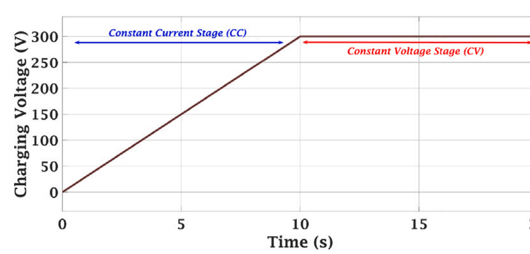

Fig. 24. Battery charging voltage; state $x_9=V_b(G2V\,mode)$.

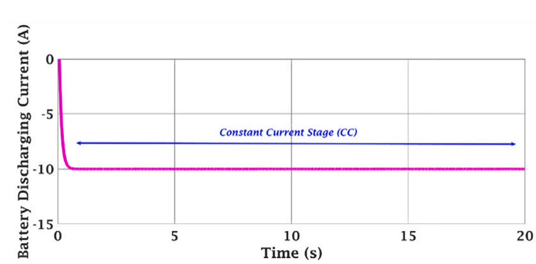

Fig. 25. Battery discharge current; $I_b(V2G\,mode)$.

from 55 A to 35 A at $t = 16 - 20$ s the UC in Fig. 21 is neutralized. The perfect tracking of reference currents of HESS defines effectiveness of proposed controller. Ultimately, the SoC's of battery and UC presented in Fig. 22 revealed that both devices are in true correspondence with their charge–discharge pattern. The value of SoC has been kept within the finite limit of 0 and 1.

4.2. Results and analysis of grid connected EV charger

Simulation parameters of EV charger have been mentioned in Table 6. In Figs. 23 and 24 charging process of BEV during G2V mode has been presented. During *CC* stage, constant 10 A current has been fed to BEV and voltage of battery V_b uniformly increases to its reference value 300 V. After $t = 20$ s *CV* stage is actuated and the battery current I_b start decaying whereas V_b becomes constant.

Similarly, discharging process of BEV during V2G mode has been illustrated in Figs. 25 and 26. Discharging of battery has been carried out by setting the reference for battery current $I_b = -10$ A during *CC* stage as presented in Fig. 25. Battery voltage V_b can be seen in Fig. 26 decreasing gradually, depicting the discharging process of battery of EV during V2G mode of operation.

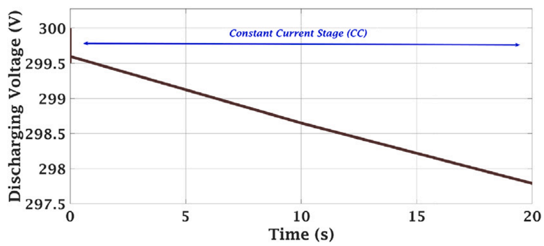

Fig. 26. Battery discharging voltage; state $x_9=V_b(V2Gmode)$.

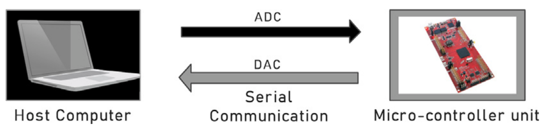

Fig. 27. HIL schematics.

5. Experimental results

The performance of proposed nonlinear controller for the DC bus voltage regulation of DCMG has been validated in the real time environment by hardware in loop (HIL) setup as shown in Fig. 27. Micro-controller unit (MCU) MS320F28379D Dual-Core Delfino™ has been used for implementing the proposed controller to generate the PWM signals for DC–DC power converters. Specifications of both host computer and MCU have been listed in Table 7. The DCMG model has been simulated in MATLAB/Simulink and the controller part has been deployed to MCU using "Embedded Coder Support Package for Texas Instruments C2000 Processors". MCU is responsible for generating the control signals for the switching of DC–DC power converters based on the control laws with the switching frequency of 25 kHz. Digital to analogue converter (DAC) converts the digital output of controller in analogue signal which is then transmitted to the host computer using universal asynchronous receiver and transmitter (UART). In return the analogue signal from the host computer is received by UART and then converted into digital input by analogue to digital converter (ADC) to make it readable for the MCU. This forms a closed loop between the host computer and MCU using a built in 16-bit ADC and DAC and the serial communication interface is established in real time environment. To make the HIL experiment elementary the power of RESs and FC have been kept constant. Both the cases of constant and varying load current have been tested in real time environment and the results then compared with those of simulation.

5.1. Experimental verification of HESS

5.1.1. Case-I

Under the constant load current, regulated output DC bus voltage has been shown in Fig. 28. A steady state error can be seen but it is negligible as it is in the rated range of operation. A little Quantization noise due to the UART serial communication interface established between host computer and MCU can be seen in Figs. 29 and 30. This is due to the fact that analogue signal keep on changing and regularity is not found in the digital signal during analogue to digital conversion. Nevertheless it shows an efficient reference current tracking of battery and UC respectively in HIL environment.

5.1.2. Case-II

Under the varying load condition, regulated output DC bus voltage has been shown in Fig. 31. Some transients are there at $t = 24.5$, 29.5, 33.5 and 38 s. These are due to the variation in load demand and charge–discharge process of both the battery and UC. Experimental results of the current tracking of battery and UC in Figs. 32 and 33 are in well correspondence to the simulation results. This depicts an excellent performance of the proposed controller.

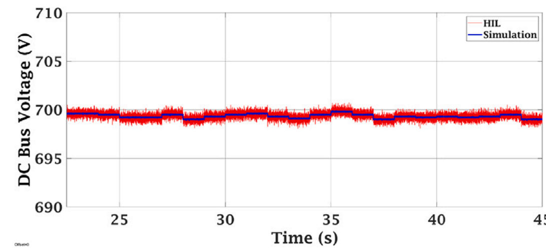

Fig. 28. Case 1: DC bus voltage (state $x_7=V_{dc}$).

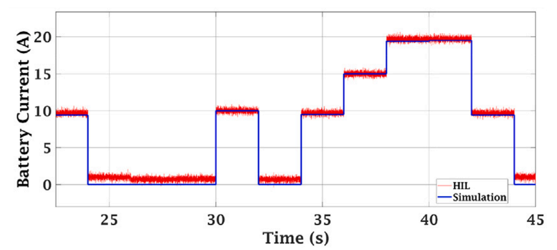

Fig. 29. Case 1: Battery current (state $x_5=I_{bat}$).

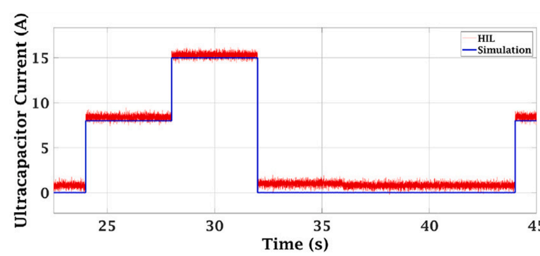

Fig. 30. Case 1: Ultracapacitor current (state $x_6=I_{uc}$).

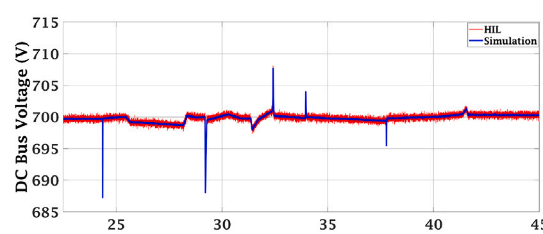

Fig. 31. Case 2: DC bus voltage (state $x_7=V_{dc}$).

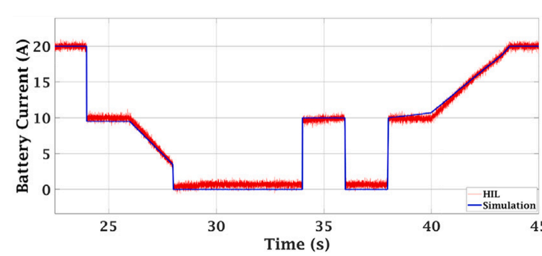

Fig. 32. Case 2: Battery current (state $x_5=I_{bat}$).

6. Conclusion

In this research work, renewable energy and hybrid energy storage system based DC microgrid alongwith grid connected BEV charger have been presented. ANN algorithm has been used for MPPT in PV energy system and the results have been found very close to the target

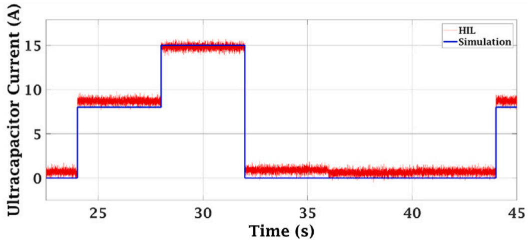

Fig. 33. Case 2: Ultracapacitor current (state $x_6 = I_{uc}$).

Table 5
Parameters of simulated DC microgrid.

Configuration	
DC grid nominal voltage	700 V
DC bus capacitor C_{dc}	68 μF
DC-DC converters	
Inductances	
L_w, L_{pv}	20 mH, 20 mH
L_{fc}, L_{bat}, L_{uc}	3.3 mH, 3.3 mH, 3.3 mH
Capacitances	
C_w, C_{pv}, C_{dc}	68 μF, 68 μF, 68 μF
Control parameters	
ρ_1, ρ_2, ρ_3	200, 1000, 1500
ρ_4, ρ_5, ρ_6	250, 250, 150
k_1, k_2, k_3	0.1, 0.1, 0.3
k_4, k_5, k_6	0.3, 0.3, 0.1
γ_1, γ_2, γ_3	1.5, 1.5, 1.5
γ_4, γ_5, γ_6	1.5, 1.5, 1.5

Table 6
Parameters of grid connected BEV charger.

Battery connected DC–DC converter	
Battery side inductor L	1.5 mH
Battery side capacitor C	700 μF
Battery full charge voltage	300 V
Battery EPR R_p	1000 Ω
Battery ESR R_b	0.06 Ω
Battery capacitance C_b	500 F
Control parameters	
c_7	10
c_8	1000

Table 7
HIL setup specifications.

Micro-controller specifications	
Micro-controller unit	TMS320F28379D
Micro processor	C2000
Operating system	32 bit
Frequency	200 MHz
Flash memory	1024 kB
RAM	204 kB
Total Processing	800 MIPS
ADC resolution	16 bit
UART	4
CAN	2
PWM	24 channel
Notebook specifications	
Micro processor	10510U
Core	i7
Operating system	64 bit
Frequency	1.8 GHz
ROM	512 GB
RAM	16 GB

values. DC bus voltage regulation of DCMG have been carried out using ITSMC which depicts an efficient performance against SMC and Lyapunov redesign control. The proposed controller also maintained an efficient power balance between RESs and HESS. Whereas, Backstepping controller has been implemented for the G2V and V2G modes of operation in grid connected BEV charger. Lyapunov analysis verified the asymptotic stability of the whole system. The proposed controllers have been implemented in MATLAB/Simulink^R (2020b) to substantiate the performance of the whole system against load transients. Controller hardware in loop analysis ensured the practical applicability of the proposed controller in real time environment. The future aim of this research work lies in the parametric optimization by using an appropriate optimization algorithm. Other nonlinear controllers might be used in grid connected mode to further improve the performance of DCMG. The considered topology would be tested in operational horizon by proposing an efficient energy management system incorporating the cost based discomfort index of consumer.

CRediT authorship contribution statement

Hafiz Muhammad Mehdi: Conceptualization, Methodology, Software, Formal analysis, Writing – original draft, Visualization. **Muhammad Kashif Azeem:** Software, Investigation, Writing – original draft. **Iftikhar Ahmad:** Supervision, Data curation, Writing – review & editing, Validation.

Declaration of competing interest

The authors declare that they have no known competing financial interests or personal relationships that could have appeared to influence the work reported in this paper.

Data availability

No data was used for the research described in the article.

References

[1] S.R. Bull, Renewable energy today and tomorrow, Proc. IEEE 89 (8) (2001) 1216–1226.

[2] C.L. Benson, C.L. Magee, On improvement rates for renewable energy technologies: Solar PV, wind turbines, capacitors, and batteries, Renew. Energy 68 (2014) 745–751.

[3] A. Bari, J. Jiang, W. Saad, A. Jaekel, Challenges in the smart grid applications: an overview, Int. J. Distrib. Sens. Netw. 10 (2) (2014) 974682.

[4] A. Armghan, M.K. Azeem, H. Armghan, M. Yang, F. Alenezi, M. Hassan, Dynamical operation based robust nonlinear control of DC microgrid considering renewable energy integration, Energies 14 (13) (2021) 3988.

[5] S.S. Zehra, A.U. Rahman, H. Armghan, I. Ahmad, U. Ammara, Artificial intelligence-based nonlinear control of renewable energies and storage system in a DC microgrid, ISA Trans. (2021).

[6] H. Armghan, M. Yang, A. Armghan, N. Ali, M. Wang, I. Ahmad, Design of integral terminal sliding mode controller for the hybrid AC/DC microgrids involving renewables and energy storage systems, Int. J. Electr. Power Energy Syst. 119 (2020) 105857.

[7] W. Jing, C.H. Lai, S.H.W. Wong, M.L.D. Wong, Battery-supercapacitor hybrid energy storage system in standalone DC microgrids: areview, IET Renew. Power Gener. 11 (4) (2017) 461–469.

[8] R.A. Dougal, S. Liu, R.E. White, Power and life extension of battery-ultracapacitor hybrids, IEEE Trans. Compon. Packag. Technol. 25 (1) (2002) 120–131.

[9] M. Arsalan, R. Iftikhar, I. Ahmad, A. Hasan, K. Sabahat, A. Javeria, MPPT for photovoltaic system using nonlinear backstepping controller with integral action, Sol. Energy 170 (2018) 192–200.

[10] A. El Khateb, N. Abd Rahim, J. Selvaraj, M.N. Uddin, Fuzzy-logic-controller-based SEPIC converter for maximum power point tracking, IEEE Trans. Ind. Appl. 50 (4) (2014) 2349–2358.

[11] S. Ahmed, H.M. Muhammad Adil, I. Ahmad, M.K. Azeem, S. Abbas Khan, et al., Supertwisting sliding mode algorithm based nonlinear MPPT control for a solar PV system with artificial neural networks based reference generation, Energies 13 (14) (2020) 3695.

[12] H. Kakigano, M. Nomura, T. Ise, Loss evaluation of DC distribution for residential houses compared with AC system, in: The 2010 International Power Electronics Conference-ECCE ASIA, IEEE, 2010, pp. 480–486.

[13] A. Alanazi, H. Lotfi, A. Khodaei, Coordinated AC/DC microgrid optimal scheduling, in: 2017 North American Power Symposium, NAPS, IEEE, 2017, pp. 1–6.
[14] A.T. Elsayed, A.A. Mohamed, O.A. Mohammed, DC microgrids and distribution systems: An overview, Electr. Power Syst. Res. 119 (2015) 407–417.
[15] J. Rocabert, A. Luna, F. Blaabjerg, P. Rodriguez, Control of power converters in AC microgrids, IEEE Trans. Power Electron. 27 (11) (2012) 4734–4749.
[16] J. Kim, J.M. Guerrero, P. Rodriguez, R. Teodorescu, K. Nam, Mode adaptive droop control with virtual output impedances for an inverter-based flexible AC microgrid, IEEE Trans. Power Electron. 26 (3) (2010) 689–701.
[17] H. Han, X. Hou, J. Yang, J. Wu, M. Su, J.M. Guerrero, Review of power sharing control strategies for islanding operation of AC microgrids, IEEE Trans. Smart Grid 7 (1) (2015) 200–215.
[18] H. Cai, G. Hu, F.L. Lewis, A. Davoudi, A distributed feedforward approach to cooperative control of AC microgrids, IEEE Trans. Power Syst. 31 (5) (2015) 4057–4067.
[19] J.M. Guerrero, J.C. Vasquez, J. Matas, L.G. De Vicuña, M. Castilla, Hierarchical control of droop-controlled AC and DC microgrids—A general approach toward standardization, IEEE Trans. Ind. Electron. 58 (1) (2010) 158–172.
[20] H. Kakigano, Y. Miura, T. Ise, Distribution voltage control for DC microgrids using fuzzy control and gain-scheduling technique, IEEE Trans. Power Electron. 28 (5) (2012) 2246–2258.
[21] M. Babazadeh, H. Karimi, A robust two-degree-of-freedom control strategy for an islanded microgrid, IEEE Trans. Power Deliv. 28 (3) (2013) 1339–1347.
[22] M. Kumar, S. Srivastava, S. Singh, Control strategies of a DC microgrid for grid connected and islanded operations, IEEE Trans. Smart Grid 6 (4) (2015) 1588–1601.
[23] X. Lu, J.M. Guerrero, K. Sun, J.C. Vasquez, An improved droop control method for DC microgrids based on low bandwidth communication with DC bus voltage restoration and enhanced current sharing accuracy, IEEE Trans. Power Electron. 29 (4) (2013) 1800–1812.
[24] Y.A.-R.I. Mohamed, H.H. Zeineldin, M. Salama, R. Seethapathy, Seamless formation and robust control of distributed generation microgrids via direct voltage control and optimized dynamic power sharing, IEEE Trans. Power Electron. 27 (3) (2011) 1283–1294.
[25] S. Singh, D. Fulwani, V. Kumar, Robust sliding-mode control of dc/dc boost converter feeding a constant power load, IET Power Electron. 8 (7) (2015) 1230–1237.
[26] M.D. Cook, G.G. Parker, R.D. Robinett, W.W. Weaver, Decentralized mode-adaptive guidance and control for DC microgrid, IEEE Trans. Power Deliv. 32 (1) (2016) 263–271.
[27] S. Neisarian, M.M. Arefi, N. Vafamand, M. Javadi, S.F. Santos, J.P. Catalão, Finite-time adaptive sliding mode control of DC microgrids with constant power load, in: 2021 IEEE Madrid PowerTech, IEEE, 2021, pp. 1–6.
[28] T.K. Roy, M.A. Mahmud, A.M.T. Oo, M.E. Haque, K.M. Muttaqi, N. Mendis, Nonlinear adaptive backstepping controller design for islanded DC microgrids, IEEE Trans. Ind. Appl. 54 (3) (2018) 2857–2873.
[29] M. Cupelli, M. Moghimi, A. Riccobono, A. Monti, A comparison between synergetic control and feedback linearization for stabilizing MVDC microgrids with constant power load, in: IEEE PES Innovative Smart Grid Technologies, Europe, IEEE, 2014, pp. 1–6.
[30] A. Iovine, M.J. Carrizosa, G. Damm, P. Alou, Nonlinear control for DC microgrids enabling efficient renewable power integration and ancillary services for AC grids, IEEE Trans. Power Syst. 34 (6) (2018) 5136–5146.
[31] M.A. Jarrahi, F. Roozitalab, M.M. Arefi, M.S. Javadi, J.P. Catalao, DC microgrid energy management system containing photovoltaic sources considering supercapacitor and battery storages, in: 2020 International Conference on Smart Energy Systems and Technologies, SEST, IEEE, 2020, pp. 1–6.
[32] M.I. Ghiasi, M.A. Golkar, A. Hajizadeh, Lyapunov based-distributed fuzzy-sliding mode control for building integrated-DC microgrid with plug-in electric vehicle, IEEE Access 5 (2017) 7746–7752.
[33] M. Hossain, H.R. Pota, M.A. Mahmud, M. Aldeen, Robust control for power sharing in microgrids with low-inertia wind and PV generators, IEEE Trans. Sustain. Energy 6 (3) (2014) 1067–1077.
[34] J. Hu, Y. Shan, Y. Xu, J.M. Guerrero, A coordinated control of hybrid ac/dc microgrids with PV-wind-battery under variable generation and load conditions, Int. J. Electr. Power Energy Syst. 104 (2019) 583–592.
[35] M.A. Abdullah, A. Yatim, C.W. Tan, R. Saidur, A review of maximum power point tracking algorithms for wind energy systems, Renew. Sustain. Energy Rev. 16 (5) (2012) 3220–3227.
[36] N. Tashakor, E. Farjah, T. Ghanbari, A bidirectional battery charger with modular integrated charge equalization circuit, IEEE Trans. Power Electron. 32 (3) (2016) 2133–2145.
[37] M. Restrepo, J. Morris, M. Kazerani, C.A. Canizares, Modeling and testing of a bidirectional smart charger for distribution system EV integration, IEEE Trans. Smart Grid 9 (1) (2016) 152–162.
[38] L. Pan, C. Zhang, An integrated multifunctional bidirectional AC/DC and DC/DC converter for electric vehicles applications, Energies 9 (7) (2016) 493.
[39] V. Monteiro, J.G. Pinto, J.L. Afonso, Experimental validation of a three-port integrated topology to interface electric vehicles and renewables with the electrical grid, IEEE Trans. Ind. Inform. 14 (6) (2018) 2364–2374.
[40] V. Monteiro, J. Pinto, J.L. Afonso, Operation modes for the electric vehicle in smart grids and smart homes: Present and proposed modes, IEEE Trans. Veh. Technol. 65 (3) (2015) 1007–1020.
[41] M. Garcés Quílez, M. Abdel-Monem, M. El Baghdadi, Y. Yang, J. Van Mierlo, O. Hegazy, Modelling, analysis and performance evaluation of power conversion unit in g2v/v2g application—A review, Energies 11 (5) (2018) 1082.
[42] K. Sayed, H.A. Gabbar, Electric vehicle to power grid integration using three-phase three-level AC/DC converter and PI-fuzzy controller, Energies 9 (7) (2016) 532.
[43] A. Rachid, H. El Fadil, F. Giri, Dual stage CC-CV charge method for controlling dc-dc power converter in BEV charger, in: 2018 19th IEEE Mediterranean Electrotechnical Conference, MELECON, IEEE, 2018, pp. 74–79.
[44] M. Nasiri, J. Milimonfared, S. Fathi, Modeling, analysis and comparison of TSR and OTC methods for MPPT and power smoothing in permanent magnet synchronous generator-based wind turbines, Energy Convers. Manage. 86 (2014) 892–900.
[45] H. Armghan, M. Yang, M. Wang, N. Ali, A. Armghan, Nonlinear integral backstepping based control of a DC microgrid with renewable generation and energy storage systems, Int. J. Electr. Power Energy Syst. 117 (2020) 105613.
[46] Z. e Huma, M.K. Azeem, I. Ahmad, H. Armghan, S. Ahmed, H.M.M. Adil, Robust integral backstepping controller for energy management in plugin hybrid electric vehicles, J. Energy Storage 42 (2021) 103079.
[47] M.S. Javadi, A.E. Nezhad, P.H. Nardelli, M. Gough, M. Lotfi, S. Santos, J.P. Catalão, Self-scheduling model for home energy management systems considering the end-users discomfort index within price-based demand response programs, Sustainable Cities Soc. 68 (2021) 102792.
[48] M.S. Javadi, M. Gough, M. Lotfi, A.E. Nezhad, S.F. Santos, J.P. Catalão, Optimal self-scheduling of home energy management system in the presence of photovoltaic power generation and batteries, Energy 210 (2020) 118568.
[49] M. Lotfi, T. Almeida, M.S. Javadi, G.J. Osório, C. Monteiro, J.P. Catalão, Coordinating energy management systems in smart cities with electric vehicles, Appl. Energy 307 (2022) 118241.